ACS OMEGA

http://pubs.acs.org/journal/acsodf

Article

# Raman Anisotropy and Polarization-Sensitive Photodetection in 2D $Bi_2O_2Se$–$WSe_2$ Heterostructure

Lin Tao,[#] Sina Li,[#] Bin Yao,* Mengjia Xia, Wei Gao, Yujue Yang,* Xiaozhou Wang,* and Nengjie Huo*

Cite This: *ACS Omega* 2021, 6, 34763–34770

Read Online

ACCESS | Metrics & More | Article Recommendations | Supporting Information

**ABSTRACT:** Two-dimensional (2D) bismuth oxyselenide ($Bi_2O_2Se$) has attracted increasing attention due to its high mobility, tunable band gap, and air stability. The surface reconstruction of cleaved $Bi_2O_2Se$ due to the electrostatic interlayer interactions can lead to the in-plane anisotropic structure and physics. In this work, we first discovered the strong anisotropy in phonon modes through the angle-resolved polarized Raman (ARPR) spectra. Benefiting from the anisotropic feature, a high-performance polarization-sensitive photodetector has been achieved by constructing a heterostructure composed of the multilayer $Bi_2O_2Se$ as polarized-light sensitizers and 2D $WSe_2$ as a photocarrier transport channel. The detectors exhibit broadband response spectra from 405 to 1064 nm along with high responsivity, fast speed, and high sensitivity owing to the photogating effect in this device architecture. More importantly, the photocurrent shows strong light polarization dependence with the maximum dichroism ratio of 4.9, and a reversal is observed for the angle-dependent photocurrent excited by polarized 405 and 635 nm light. This work provides new insight in terms of optical and photocurrent anisotropy of exfoliated $Bi_2O_2Se$ and expands its applications in angle-resolved electronics and optoelectronics.

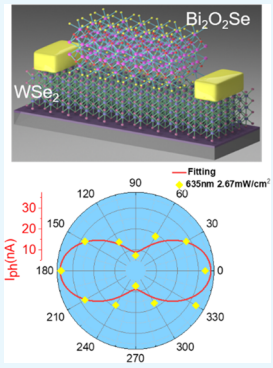


## INTRODUCTION

For the two-dimensional (2D) materials with an in-plane anisotropic crystalline structure, the electronic and band structures show high dependence on orientations, leading to the strong anisotropy in effective mass, optical absorption, and electrical transport, giving rise to the unique feature of linear dichroism in these classes of materials.[1−7] The linear dichroism endows them as promising platforms for angle-resolved optoelectronic applications such as polarization spectroscopy imaging, polarized photodetectors, and optical radar.[8−10] In the past, the optical media with meta-surface structures has been widely utilized to manipulate the light phase and polarization,[11] while the complex and costly manufacturing process is the limiting factor for practical applications. Due to the geometric anisotropy, the one-dimensional (1D) nanowires or nanobelts such as ZnO, InP, and $Sb_2S_3$ can also exhibit the linear dichroism effect and capability of polarization photodetection; however, the small aspect ratios hamper the dichroism ratio and limit the diversity of device fabrication.[12−14]

Recently, the low-symmetric 2D materials have emerged as centers for polarization-dependent optical and electrical applications due to their intrinsic in-plane anisotropic properties.[1] For example, the black phosphorus (b-P) with a puckered honeycomb structure has shown the distinct anisotropy in optical absorption, photoluminescence (PL), carrier mobility, and thermoelectric transport,[6,15,16] realizing the polarization-sensitive photodetectors, field-effect transistors, etc. Inspired by the anisotropic feature of b-P, the black arsenic (b-As) from the same group V was also reported to exhibit in-plane optical and electrical anisotropy with a dichroism ratio of 2.68 in electron mobility.[17] In addition, the germanium selenide (GeSe),[18] germanium arsenic (GeAs),[19] and low-symmetry transition-metal dichalcogenides (TMDs) such as $T_d$-$WTe_2$,[20] 1T-$MoTe_2$,[21] $ReS_2$,[22] and $ReSe_2$[23] have also been established as anisotropic material systems possessing strong linear dichroism. On the other hand, highly symmetric 2D materials such as graphene and 2H-TMDs with a hexagonal crystal structure have been regarded as in-plane isotropy lacking the potential in polarization-dependent applications.

As new emerging 2D ternary materials, layered bismuth oxyselenide ($Bi_2O_2Se$) has been rapidly developed with great success in electronic and optoelectronic applications including field-effect transistors, near-infrared photodetectors, thermal electronics, and topological quantum devices, benefitting from their ultrahigh mobility, outstanding stability, and tunable band gaps.[24] The electron mobility can reach as high as 20 000 $cm^2/(V\ s)$ at low temperature and 450 $cm^2/(V\ s)$ at room temperature, enabling the detection of Shubnikov–de Haas quantum oscillations.[25,26] The corresponding photodetectors exhibited broadband, highly sensitive, and ultrafast photodetection performance from near-infrared to terahertz.[27] Although a fascinating development, the linear dichroism and

Received: September 21, 2021
Accepted: November 29, 2021
Published: December 12, 2021

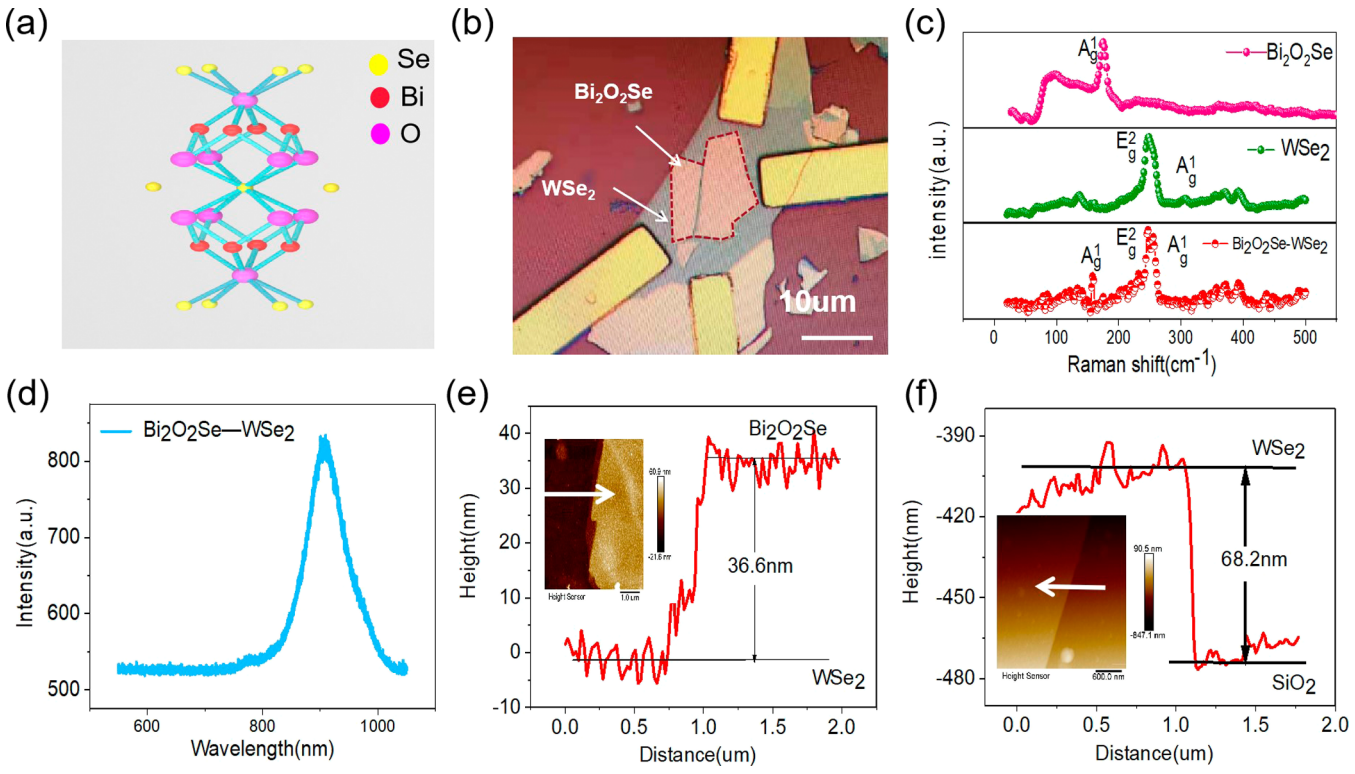


**Figure 1.** (a) Atomic structure of $Bi_2O_2Se$. (b) Optical microscopy (OM) image of the device based on the $Bi_2O_2Se/WSe_2$ heterostructure. (c) Raman spectra of the heterostructure and the components. (d) PL spectral of the heterostructures. (e, f) Atomic force microscopy (AFM) image and thickness profile of $Bi_2O_2Se$ and $WSe_2$ layers.

polarized electronics based on $Bi_2O_2Se$ have been rarely studied and remain elusive.

As we know, $Bi_2O_2Se$ belongs to a body-centered tetragonal phase ($I4/mmm$) group with strong anisotropy, consisting of positively charged $[Bi_2O_2]_n^{2n+}$ layers that are alternately sandwiched with the negatively charged $[Se]_n^{2n-}$, as shown in Figure 1a. Different from other van der Waals (vdW) layer materials, the interaction between $[Bi_2O_2]_n^{2n+}$ and $[Se]_n^{2n-}$ is the electrostatic force instead of vdW force,[28] making it hard to be mechanically exfoliated. Currently, the chemical vapor deposition (CVD) method is the most common approach to obtain the thin and large-area $Bi_2O_2Se$ with the lateral size of up to hundreds of micrometers.[25,29,30] We note that the CVD-grown samples have atomically smooth surfaces; in contrast, the $Bi_2O_2Se$ samples obtained through the cleavage method show a complicated surface reconstruction due to the existence of interlayer electrostatic interactions, which led to the difference in surface morphology and band structure.[31] When the crystal is mechanically cleaved, 50% of the Se atoms are attached to each Bi plane because of the electroneutrality requirement.[32] Through the scanning tunneling spectroscopy, the interlinked weave pattern of Se vacancies and morphology of steps have been observed on the $Bi_2O_2Se$ surface,[32] which can offer an opportunity for exploring unique physical properties and device functionality. For example, the strong surface reconstruction due to the interlayer electrostatic force can result in a remarkable spontaneous in-plane anisotropy and electric polarization.[33]

In this work, we prepared the multilayer $Bi_2O_2Se$ using the mechanically exfoliated method. Through the angle-resolved polarized Raman spectroscopy (ARPR), we first discovered the significant anisotropic Raman modes of the exfoliated $Bi_2O_2Se$. The intensities of Raman modes show a marked periodic feature (180°) with a two-lobed shape. Furthermore, $Bi_2O_2Se$ as a photosensitive layer has been integrated with $WSe_2$ layers acting as a photocarrier channel, the constructed heterostructures exhibit high polarization-sensitive photodetection performance. The dichroism ratio of photocurrent for 405 and 635 nm light can reach 2.2 and 4.9, respectively. It is interesting that the orientations at which the photocurrent under 405 and 635 nm polarized light reach the maximum are 0 and 90°, respectively, implying the optical reversal of linear dichroism when switching light from 405 to 635 nm. This is consistent with the predicted polarization-resolved absorption spectra where the linear dichroism reversal also occurs.[33] Due to the photogating effect at the interface and a suitable band gap of $Bi_2O_2Se$, the devices also exhibit broadband photoresponse ranging from 405 to 1064 nm with a high responsivity of 44 A/W, fast speed of less than 20 ms, and high detectivity of up to $3 \times 10^{13}$ Jones. The first observation of Raman anisotropy and high-performance polarized-light photodetection can make layered $Bi_2O_2Se$ promising candidates for angle-dependent optoelectronic applications.

## RESULTS AND DISCUSSION

The multilayer $Bi_2O_2Se$ was exfoliated on the $Si/SiO_2$ substrate and then transferred on top of the $WSe_2$ layers (Figure 1b). The clear diffraction selected area electron diffraction (SAED) pattern is observed (Figure S1), demonstrating the high crystalline quality of the $Bi_2O_2Se$ nanosheets. The detailed process can be seen in the Experimental Section. The purpose of constructing the heterostructure is to form the out-of-plane built-in field at the interface, inducing the photogating effect for highly efficient photodetection, which will be discussed


https://doi.org/10.1021/acsomega.1c05246
ACS Omega 2021, 6, 34763−34770

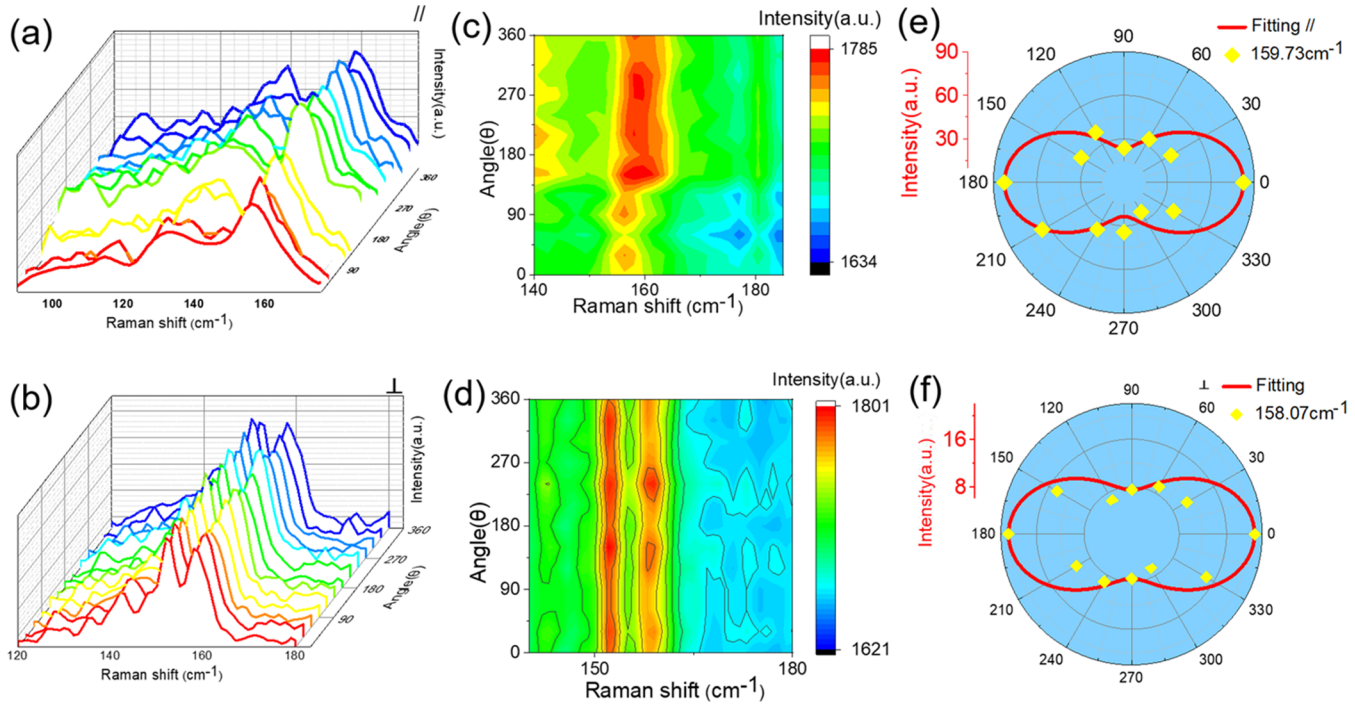


**Figure 2.** (a, b) Raman spectra of $Bi_2O_2Se$ at different rotation angles under the parallel and cross-polarized configuration, respectively. (c, d) Polarized Raman mapping and (e, f) plots in polar coordinate at the varying rotation angles from 0 to 330° under parallel and cross-polarization configuration, respectively.

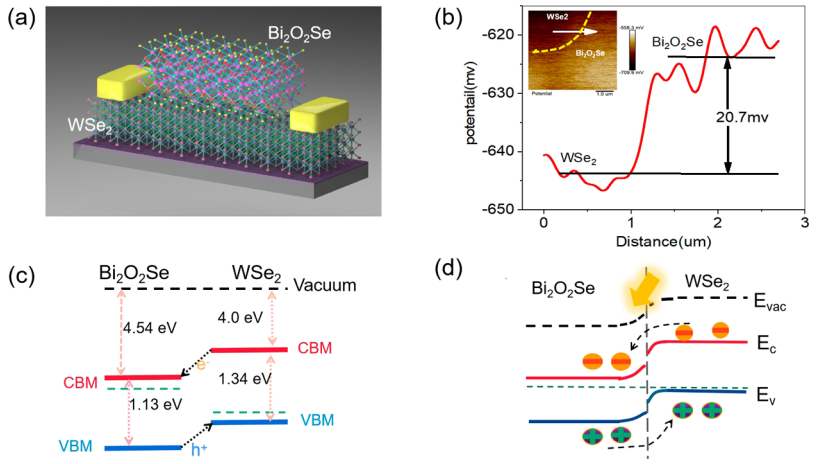


**Figure 3.** (a) Schematic diagram of $Bi_2O_2Se/WSe_2$ heterostructure devices. (b) KPFM of the heterostructure at the interface. (c, d) Band diagram of the heterostructure before and after contact, respectively.

later. Figure 1c shows the Raman spectra of $Bi_2O_2Se$, $WSe_2$, and their heterostructures. The Raman peaks located at 158.8 and 252 $cm^{-1}$ are ascribed to the $A_{1g}$ mode of $Bi_2O_2Se$ and $WSe_2$, respectively, which is consistent with previous reports.[34,35] The PL spectrum was obtained under the excitation of a 532 nm laser, showing a strong PL peak at 920 nm (Figure 1d), corresponding to an indirect optical band gap of multilayer $WSe_2$, while the PL is absent in $Bi_2O_2Se$ layers. In the heterostructures, the thickness of the $Bi_2O_2Se$ and $WSe_2$ layers is 36.6 and 68.2 nm from AFM images as shown in Figure 1e,f, respectively.

Angle-resolved polarized Raman spectroscopy (ARPR) has been regarded as a facile technique to identify the anisotropic crystal structure. To further investigate the crystal structure symmetry and the electron−phonon interactions on the surface of $Bi_2O_2Se$, we performed the ARPR measurement with both parallel and cross-polarization configurations. To realize this, we inserted a linear polarizer in front of the Raman detection system and detected the scattered light along the parallel or perpendicular to the incident light polarization. The ARPR was measured by rotating the sample with 30° steps. The rotation angle $\theta$ is defined as the angle between the $a$-axis and laser polarization direction, and Figure S2 shows the optical microscopy images of the $Bi_2O_2Se$ sample under each rotation angle from 0 to 330°. Figure 2a,b shows the Raman spectra for $Bi_2O_2Se$ at different rotation angles under the parallel or cross-polarized configuration, respectively. Figure 2c,d shows the polarized Raman mapping at different rotation angles from 0 to 330° under parallel and cross-polarization configuration, respectively. Under the parallel configuration,


https://doi.org/10.1021/acsomega.1c05246
ACS Omega 2021, 6, 34763−34770

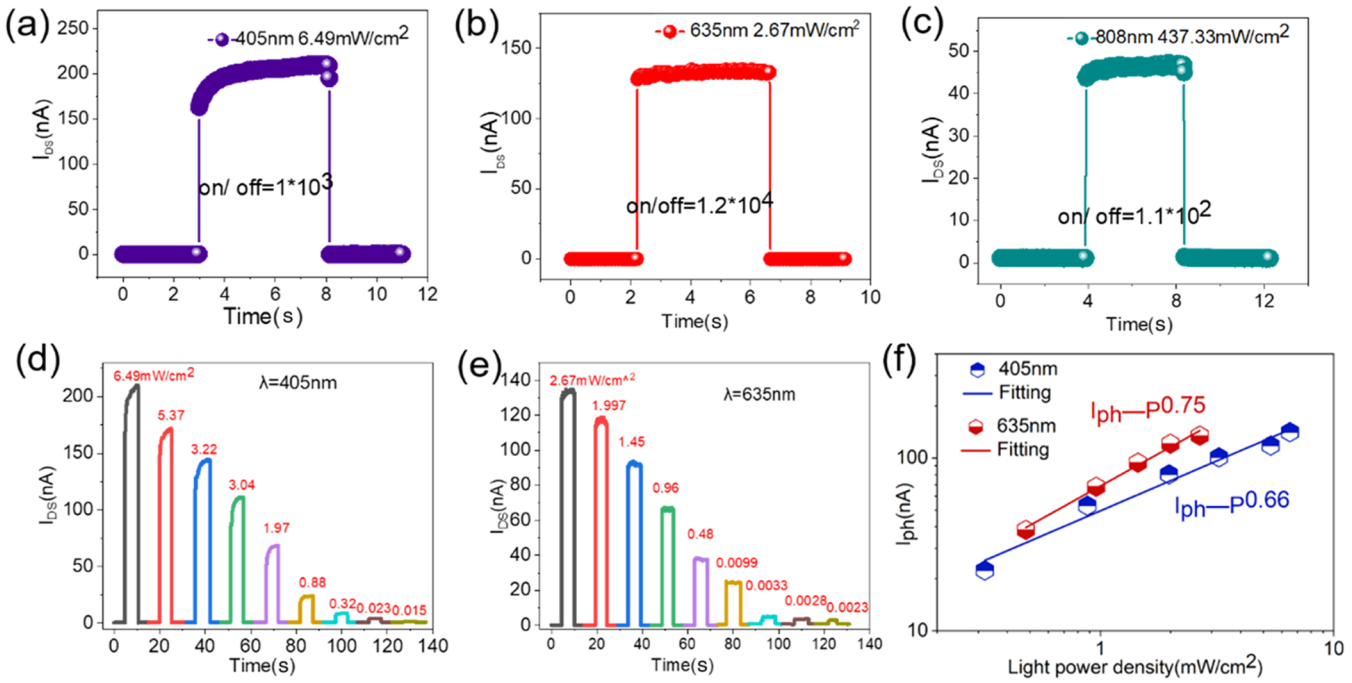


**Figure 4.** (a–c) Dynamic photoresponse of the device under laser irradiation with wavelengths of 405, 635, and 808 nm, respectively. (d, e) Time-dependent photoresponse as a function of light power density under 405 and 635 nm light, respectively. (f) Photocurrent as a function of light power density. The solid curves are the power-law fitting.

one pronounced Raman peak at 159.7 $cm^{-1}$ is observed, while two Raman peaks at 159.73 and 158.07 $cm^{-1}$ appear under cross configuration. In both cases, we found that the intensities of these $A_{1g}$ modes present a strong correlation with rotation angles, indicating the in-plane anisotropic phonon vibration and lattice structure. The Raman intensities were then extracted to be plotted in polar coordinates as shown in Figure 2e,f. The data were well fitted using the formula

$$b(\theta) = b_{\min} \sin^2(\theta + \varphi) + b_{\max} \cos^2(\theta + \varphi)$$

where $\theta$ is the angle of the linear polarization laser. $b_{\min}$ and $b_{\max}$ are the minimum and maximum fitting parameters, respectively. The Raman intensities of $A_{1g}$ mode show a period of 180° with a two-lobed shape under both configurations. The dichroism ratios defined as the ratio of maximum intensity at 0° divided by the minimum value at 90° are 3.6 and 3.2 for parallel or cross-polarized configuration, respectively.

To further investigate the potential application of the novel linear dichroism feature, we then assembled the $Bi_2O_2Se$ nanoflakes with multilayer $WSe_2$ and fabricated the hetero-structure-based photodetectors as shown in Figure 1b. The architecture of this device is shown in Figure 3a, the underlying $WSe_2$ can act as a photocarrier transport layer and top $Bi_2O_2Se$ acts as polarization-sensitive layers. We note that the photoconductor based on individual exfoliated $Bi_2O_2Se$ has poor photoresponse due to the extremely high dark current, which can hamper the study of the polarized light detection. Thus, the purpose of constructing heterostructure structure is to introduce the photogating effect for highly efficient photodetection. Now we explain the corresponding photo-detection scheme. Through the transfer curves of the field-effect transistors based on the individual materials (Figure S3), $Bi_2O_2Se$ and $WSe_2$ exhibit n-type and p-type behavior, respectively. Thus, out-of-plane p–n junctions can form at the interface. Figure 3b shows the surface potential difference (SPD) at the interface obtained by Kelvin probe force microscopy (KPFM) measurement. The SPD between AFM tip and $Bi_2O_2Se$ ($WSe_2$) is defined as

$$\mathrm{eSPD}_{Bi_2O_2Se} = W_{tip} - W_{Bi_2O_2Se} \quad (1)$$

$$\mathrm{eSPD}_{WSe_2} = W_{tip} - W_{WSe_2} \quad (2)$$

where $W$ is the work function. The Fermi level difference ($\Delta E_F$) between $Bi_2O_2Se$ and $WSe_2$ can be calculated by the formula

$$\Delta E_F = W_{Bi_2O_2Se} - W_{WSe_2} = \mathrm{eSPD}_{WSe_2} - \mathrm{eSPD}_{Bi_2O_2Se} \quad (3)$$

Thus, $\Delta E_F$ can be calculated to be 20.7 meV. Based on the energy band and electron affinities of $Bi_2O_2Se$ and $WSe_2$,[28,36] we plot the band diagram of the heterostructure as shown in Figure 3c, depicting the type II band alignment, facilitating the charge separation. Under light illumination, the photons are absorbed by $Bi_2O_2Se$ and the excited electron–hole pairs are separated under the built-in electric field (Figure 3d). The holes are transferred into the $WSe_2$ channel layers and the electrons reside in top $Bi_2O_2Se$, resulting in the photogating effect. Within the lifetime, the holes can recirculate multiple times in the channel before recombining with electrons, leading to a large photo gain. A similar scheme is also reported in 2D/0D hybrids and 2D $MoS_2$ with an out-of-plane homojunction.[37,38]

We then performed the photodetection measurement using the lasers with different wavelength and power densities at room temperature and ambient environment. Figure 4a–c shows the dynamic photoresponse of the device under laser irradiation with wavelengths of 405, 635, and 808 nm, demonstrating a significant photocurrent and a fast response speed. The temporal response is less than 20 ms for both rise and decay processes, which can satisfy the requirement of video imaging applications. The photoswitching ratio defined


https://doi.org/10.1021/acsomega.1c05246
ACS Omega 2021, 6, 34763–34770

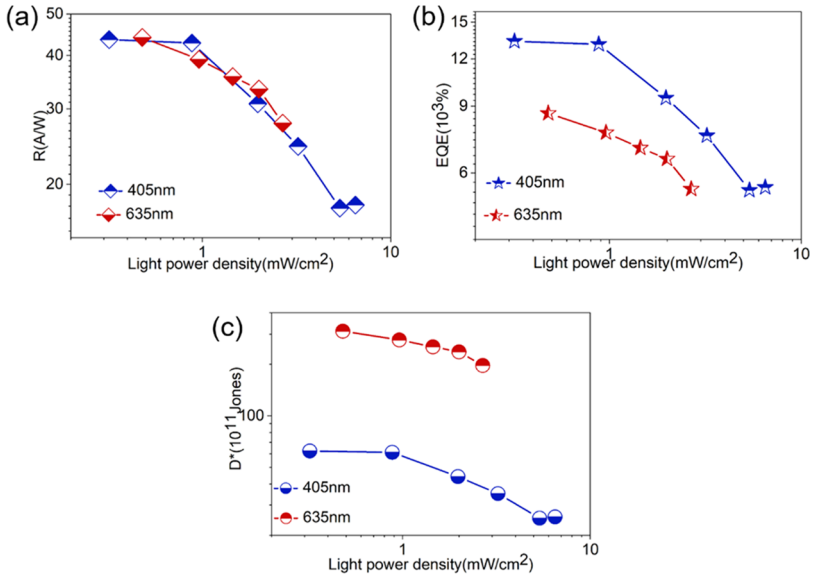


**Figure 5.** (a) Responsivity, (b) EQE, and (c) detectivity as functions of light power density for 405 and 635 nm light.

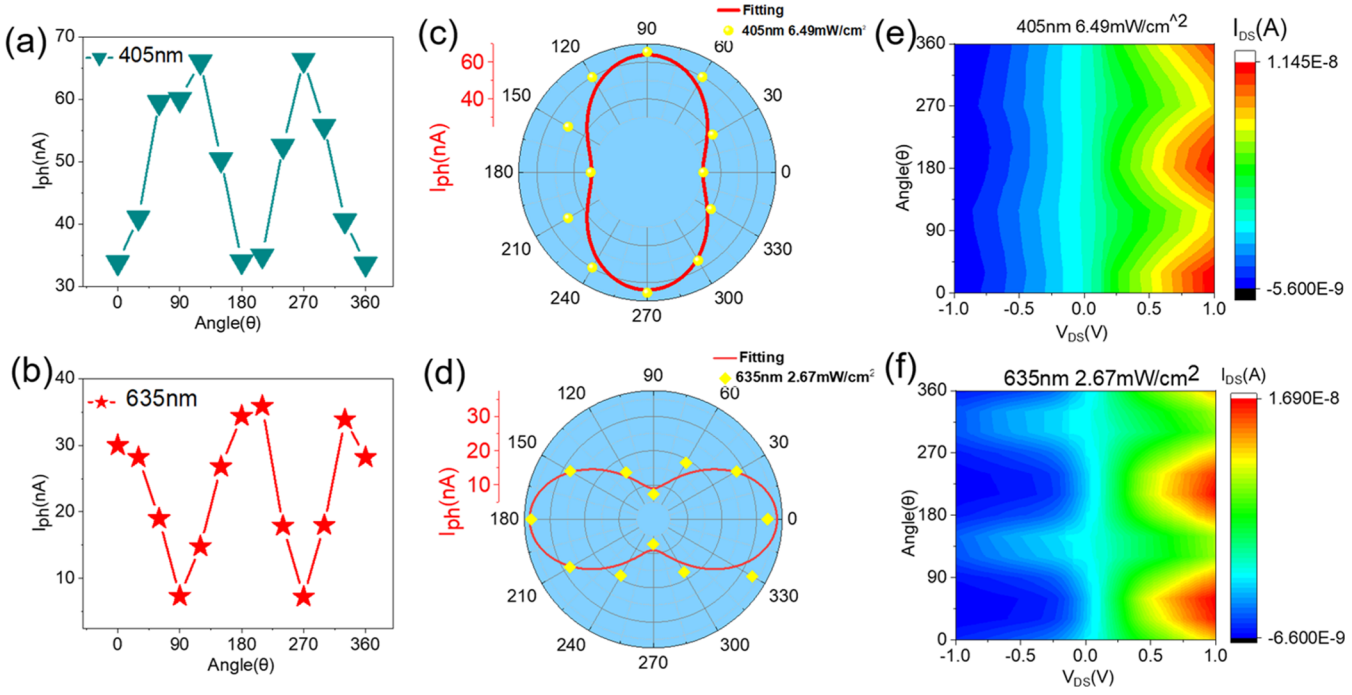


**Figure 6.** (a, b) Photocurrent as a function of polarization angles for the 405 and 635 nm light. (c, d) Same as (a, b) but in polar coordinates. (e, f) Mapping plot of $I-V$ curves at 405 and 635 nm light with varying light polarization angles.

as $I_{light}/I_{dark}$ can reach $10^3$ and $10^4$ for 405 and 635 nm light, respectively, as a result of low dark current, implying a high sensitivity. The device can also respond to the near-infrared laser with wavelength of 980 and 1064 nm as shown in Figure S4 (Supporting Information) due to the small band gap of $Bi_2O_2Se$ layers, indicating a broad spectral coverage from 405 to 1064 nm. In addition, the photocurrent mapping of the photodetector is also measured (Figure S5), showing the strong photocurrent at the area between drain electrodes and the $Bi_2O_2Se$ layer.

The measured time-dependent photoresponse as a function of light power density under 405 and 635 nm light is shown in Figure 4d,e, respectively, demonstrating gradually decreased photocurrent with decreasing light power. The photocurrent is then extracted and plotted in Figure 4f. The curves are fitted by the power-law equation of $I_{ph} \sim P^{\partial}$, where $P$ is the laser power and $\partial$ is the fitting exponent. We can see that the exponents $\partial$ are fitted to be ~0.66 and ~0.75 for 405 and 635 nm light, respectively, indicating a highly efficient conversion efficiency from incident photons to collected electron–hole pairs.

As key figures of merit for photodetectors, the responsivity ($R$), external quantum efficiency (EQE), and detectivity ($D^*$) are also evaluated as follows

$$R = I_{ph}/P \times S \tag{4}$$

$$\mathrm{EQE} = \frac{h_c \times R \times C}{e \times \lambda} \tag{5}$$



https://doi.org/10.1021/acsomega.1c05246
ACS Omega 2021, 6, 34763−34770

$$D^* = \frac{R\sqrt{S}}{\sqrt{2eI_{dark}}} \quad (6)$$

where $I_{ph}$ is the photocurrent, $S$ is the effective area of the detector, $P$ is the optical power density, $h_c$ is the Planck constant, $e$ is the unit charge, $\lambda$ is the incident wavelength, $C$ is the speed of light, and $I_{dark}$ is the dark current.

Figure 5a shows $R$ as a function of light power densities for 450 and 635 nm light. In both cases, $R$ decreases with increased light power owing to the gradual saturation of the photosensing states in the heterostructure.[38] The $R$ can reach up to 43 and 44 A/W for 405 and 635 nm, respectively, at weak light illumination. The EQE as a function of light power density is shown in Figure 5b, the maximum EQE up to $1.3 \times 10^4$ and $8.6 \times 10^3$% can be achieved for 405 and 635 nm, respectively. The high responsivity results from the huge photogain due to the existence of the photogating effect in the heterostructure as discussed above. The detectivity $D^*$ is a common figure of merit to characterize the sensitivity of a detector with the unit of cm $Hz^{1/2}$/W or Jones. The $D^*$ of the device at 405 and 635 nm light is shown in Figure 5c, which can reach up to $6.2 \times 10^{12}$ Jones at 405 nm light and $3.1 \times 10^{13}$ Jones at 635 nm light, exceeding the sensitivity of most photodetectors based on 2D materials. The $R$, EQE, and $D^*$ for the light wavelength of 808, 980, and 1064 nm as a function of light power have also been performed as shown in Figure S6, demonstrating moderate performance.

From the angle-resolved polarized Raman, $Bi_2O_2Se$ has an anisotropic in-plane crystal structure, the polarization absorption spectrum has also been measured, indicating that exfoliated $Bi_2O_2Se$ flakes have the linear dichroism in the visible light (Figure S7), which can enable a polarization-sensitive photodetection. To investigate the polarization sensitivity of the heterostructure device under the polarized light illumination, we performed the measurement using the 405 and 635 nm polarized light achieved through a polarizer. The polarization angle was varied by rotating the polarizer with 30° steps. Figure 6a,b shows photocurrent as a function of polarization angles at $V_{DS}$ of 1 V for the 405 and 635 nm light, exhibiting the periodic variations with varying polarization angles. However, the angle-varied photocurrent exhibits different phases with a difference of about 90° for the 405 and 635 nm light. Based on the data, the angle-dependent photocurrent is plotted in polar coordinates (Figure 6c,d), showing a two-lobed shape with a period of 180°, which is consistent with the periodicity of Raman modes. It is interesting that the angle at which the photocurrent reaches the maximum is 0° for 635 nm and 90° for 405 nm, which may be attributed to the reversal of linear dichroism of $Bi_2O_2Se$.[33] To further confirm the reversal of polarized photocurrent, we prepared other heterostructures with thicker $Bi_2O_2Se$. The angle-dependent photocurrents for 405 and 635 nm light are shown in Figure S8 (Supporting Information), also demonstrating polarization-sensitive photocurrent and reverse phenomenon. A similar phenomenon of reversal in optical absorption and anisotropic photocurrent has also been observed in GeAs-based polarized photodetectors.[19] The dichroism ratio of photocurrent, defined as the value of maximum photocurrent divided by the minimum photocurrent, is calculated to be 2.2 and 4.9 for 405 and 635 nm light, respectively, which implies a high polarization-sensitive performance and is at par with that of other 2D low-symmetric materials.[39−41] Figure 6e,f shows the mapping plot of $I-V$ curves at 405 and 635 nm light with varying light polarization angles, also depicting strong anisotropic photocurrent.

As control experiments, we also measured the angle-dependent photocurrent of individual $WSe_2$ devices. The photocurrent as a. function of angles is shown in polar coordinates, presenting no polarization angle dependence (Figure S9). This indicates that the $WSe_2$ component is in-plane isotropic materials, thus the anisotropic- and polarization-sensitive photocurrent of the heterostructures can be contributed from the $Bi_2O_2Se$ component.

## CONCLUSIONS

In summary, we prepared multilayer $Bi_2O_2Se$ using the mechanically exfoliated method. The intensities of phonon vibration modes show significant angle dependence with a period of 180° through the angle-resolved polarized Raman spectra, this indicates that the surface reconstruction led to the anisotropic crystal structure. We then assembled $Bi_2O_2Se$, which acted as a polarized light sensitizer with 2D $WSe_2$ layers as a photocarrier transport channel. Due to the p-type and n-type features of $WSe_2$ and $Bi_2O_2Se$, respectively, an out-of-plane p−n heterojunction can be formed, resulting in an out-of-plane built-in field that can facilitate the separation of photoexcited electron−hole pairs. As a result, superior photodetection performance in terms of high responsivity, fast speed, and high detectivity has been achieved. The detectors exhibit a broadband spectral coverage from 405 to 1064 nm. More importantly, the photoresponse of the device is also polarization-sensitive due to the linear dichroism character of the $Bi_2O_2Se$ layers. The dichroism ratio for photocurrent can reach as high as 2.2 and 4.9 for 405 and 635 nm, respectively. In addition, the photodetection performance is much superior compared to that of other reported polarization-sensitive photodetectors (Tables S1 and S2). We discovered the linear dichroism characters of exfoliated $Bi_2O_2Se$ through the ARPR and polarization absorption measurement, which is successfully utilized for polarization-sensitive photodetector applications. This work expands the family of low-symmetry 2D materials and offers a new opportunity for the development of angle-resolved electronics and optoelectronics.

## EXPERIMENTAL SECTION

**Device Fabrication of $Bi_2O_2Se/WSe_2$ Heterostructure.** Multilayer $Bi_2O_2Se$ and $WSe_2$ were achieved by the mechanical exfoliation method from the bulk crystal (purchased from Shanghai OnWay Technology Co., Ltd.) on the 300 nm $SiO_2$/Si substrate. The details of the exfoliation process can be found in the Supporting Information (Figure S10). Then, the $Bi_2O_2Se$ layer was stacked on top of the $WSe_2$ layer using the poly(vinyl alcohol) (PVA)/poly(dimethylsiloxane) (PDMS) assisted dry-transfer method. Briefly, the PVA solvent was injected on top of the PDMS placed on the glass, then the solid PVA/PDMS film was obtained by heating at 50 °C for 10 minutes. The film was stacked on $Bi_2O_2Se$. After heating at 90 °C for 5 min, the PDMS attached with $Bi_2O_2Se$ was separated from the PVA by tweezers. Then the PDMS/PVA/$Bi_2O_2Se$ film was stacked on the target $WSe_2$. Finally, the PVA can be removed by soaking in water. The contact electrodes of Ti/Au (10/60 nm) were fabricated by an ultraviolet maskless photolithography machine (TuoTuo Technology Co., Ltd.).



https://doi.org/10.1021/acsomega.1c05246
ACS Omega 2021, 6, 34763−34770

**Characterization.** Raman spectra were obtained using a confocal microscope spectrometer (Nost Technology Co., Ltd., a laser excitation of 532 nm). The thickness and surface potential differences were measured by AFM and KPFM (Dimension FastScan from Bruker Co., Ltd.). The electrical and optical characteristics were measured using a probe stage equipped with a semiconductor device analyzer (Keithley 2636B) and a four-channel laser. All of the measurements were performed in ambient conditions.

## ■ ASSOCIATED CONTENT

### Supporting Information

The Supporting Information is available free of charge at https://pubs.acs.org/doi/10.1021/acsomega.1c05246.

Transfer curves of $WSe_2$- and $Bi_2O_2Se$-based transistors, photoresponse of $Bi_2O_2Se$ and $WSe_2$ at 980 and 1064 nm light, the $R$, EQE, and $D^*$ of the device at the wavelengths of 808, 980, and 1064 nm, and polar plots of photocurrent of the thicker $Bi_2O_2Se$ and individual $WSe_2$ (PDF)

## ■ AUTHOR INFORMATION


### Corresponding Authors

**Bin Yao** − *State Key Lab of Superhard Material, and College of Physics, Jilin University, Changchun 130012, China; Key Laboratory of Physics and Technology for Advanced Batteries (Ministry of Education), College of Physics, Jilin University, Changchun 130012, China;* orcid.org/0000-0003-0748-3220; Email: binyao@jlu.edu.cn

**Yujue Yang** − *School of Physics and Optoelectronic Engineering, Guangdong University of Technology, Guangzhou 510006, China*; Email: yujue@mail.ustc.edu.cn

**Xiaozhou Wang** − *Institute of Semiconductors, South China Normal University, Guangzhou 510631, China*; Email: wxzanu@outlook.com

**Nengjie Huo** − *Institute of Semiconductors, South China Normal University, Guangzhou 510631, China; Guangdong Key Lab of Chip and Integration Technology, Guangzhou 510631, China;* orcid.org/0000-0003-2520-6243; Email: njhuo@m.scnu.edu.cn

### Authors

**Lin Tao** − *State Key Lab of Superhard Material, and College of Physics, Jilin University, Changchun 130012, China; Key Laboratory of Physics and Technology for Advanced Batteries (Ministry of Education), College of Physics, Jilin University, Changchun 130012, China*

**Sina Li** − *Institute of Semiconductors, South China Normal University, Guangzhou 510631, China*

**Mengjia Xia** − *Institute of Semiconductors, South China Normal University, Guangzhou 510631, China*

**Wei Gao** − *Institute of Semiconductors, South China Normal University, Guangzhou 510631, China;* orcid.org/0000-0002-6491-6128

Complete contact information is available at: https://pubs.acs.org/10.1021/acsomega.1c05246

### Author Contributions

#L.T. and S.L. contributed equally to this work.


### Notes

The authors declare no competing financial interest.

The data that support the findings of this study are available from the corresponding author upon request.

## ■ ACKNOWLEDGMENTS

This work is supported by the National Natural Science Foundation of China (Nos. 11904108 and 61805045) and the "The Pearl River Talent Recruitment Program" (2019ZT08X639).

## ■ REFERENCES


(1) Li, L.; Han, W.; Pi, L.; Niu, P.; Han, J.; Wang, C.; Su, B.; Li, H.; Xiong, J.; Bando, Y.; Zhai, T. Emerging in-plane anisotropic two-dimensional materials. *InfoMat* **2019**, *1*, 54−73.

(2) Xia, F.; Wang, H.; Jia, Y. Rediscovering black phosphorus as an anisotropic layered material for optoelectronics and electronics. *Nat. Commun.* **2014**, *5*, No. 4458.

(3) Ribeiro, H. B.; Pimenta, M. A.; de Matos, C. J. S.; et al. Unusual angular dependence of the Raman response in black phosphorus. *ACS Nano* **2015**, *9*, 4270−4276.

(4) Kim, J.; Lee, J. U.; Lee, J.; et al. Anomalous polarization dependence of raman scattering and crystallographic orientation of black phosphorus. *Nanoscale* **2015**, *7*, 18708−18715.

(5) Shen, W.; Hu, C.; Tao, J.; et al. Resolving the optical anisotropy of low-symmetry 2D materials. *Nanoscale* **2018**, *10*, 8329−8337.

(6) Qiao, J.; Kong, X.; Hu, Z. X.; Yang, F.; Ji, W. High-mobility transport anisotropy and linear dichroism in few-layer black phosphorus. *Nat Commun.* **2014**, *5*, No. 4475.

(7) Peng, L.; Wells, S. A.; Ryder, C. R.; Hersam, M. C.; Grayson, M. All-electrical determination of crystal orientation in anisotropic two-dimensional materials. *Phys. Rev. Lett.* **2018**, *120*, No. 086801.

(8) Zhang, E.; Wang, P.; Li, Z.; Wang, H.; Song, C.; Huang, C.; Chen, Z.; Yang, L.; Zhang, K.; Lu, S.; Wang, W.; Liu, S.; Fang, H.; Zhou, X.; Yan, H.; Zou, J.; Wan, X.; Zhou, P.; Hu, W.; Xiu, F. Tunable Ambipolar Polarization-Sensitive Photodetectors Based on High-Anisotropy $ReSe_2$ Nanosheets. *ACS Nano* **2016**, *10*, 8067−8077.

(9) Yang, H.; Jussila, H.; Autere, A.; Komsa, H.; Ye, G.; Chen, X.; Hasan, T.; Sun, Z. Optical Waveplates Based on Birefringence of Anisotropic Two-Dimensional Layered Materials. *ACS Photonics* **2017**, *4*, 3023−3030.

(10) Chen, Y.; Chen, C.; Kealhofer, R.; Liu, H.; Yuan, Z.; Jiang, L.; Suh, J.; Park, J.; Ko, C.; Zhong, M.; Wei, Z.; Li, J.; Li, S.; Gao, H.; Liu, Y.; Analytis, J.; Xia, Q.; Asensio, M.; Wu, J.; Choe, H. S.; Avila, J. Black Arsenic: A Layered Semiconductor with Extreme In-Plane Anisotropy. *Adv. Mater.* **2018**, *30*, No. 1800754.

(11) He, Q.; Sun, S.; Xiao, S.; Zhou, L. High-Efficiency Metasurfaces: Principles, Realizations, and Applications. *Adv. Opt. Mater.* **2018**, *6*, No. 1800415.

(12) Soci, C.; Zhang, A.; Xiang, B.; Dayeh, S. A.; Aplin, D.; Park, J.; et al. Zno nanowire UV photodetectors with high internal gain. *Nano Lett.* **2007**, *7*, 1003−1009.

(13) Wang, J.; Gudiksen, M.; Duan, X.; Cui, Y.; Lieber, C. Highly Polarized Photoluminescence and Photodetection from Single Indium Phosphide Nanowires. *Science* **2001**, *293*, 1455−1457.

(14) Zhong, M.; Wang, X.; Liu, S.; Li, B.; Huang, L.; Cui, Y.; Li, J.; Wei, Z. High-performance photodetectors based on $Sb_2S_3$ nanowires: wavelength dependence and wide temperature range utilization. *Nanoscale* **2017**, *9*, 12364−12371.

(15) Akahama, Y.; Endo, S.; Narita, S. Electrical Properties of Black Phosphorus Single Crystals. *J. Phys. Soc. Jpn.* **1983**, *52*, 2148−2155.

(16) Lee, S.; Yang, F.; Suh, J.; et al. Anisotropic in-plane thermal conductivity of black phosphorus nanoribbons at temperatures higher than 100 K. *Nat. Commun.* **2015**, *6*, No. 8573.

(17) Zhong, M.; Meng, H.; Liu, S.; Yang, H.; Shen, W.; Hu, C.; Yang, J.; Ren, Z.; Li, B.; Liu, Y.; He, J.; Xia, Q.; Li, J.; Wei, Z. In-Plane Optical and Electrical Anisotropy of 2D Black Arsenic. *ACS Nano* **2021**, *15*, 1701−1709.

(18) Wang, X.; Li, Y.; Huang, L.; Jiang, X. W.; Jiang, L.; Dong, H.; Wei, Z.; Li, J.; Hu, W. Short-wave near-infrared linear dichroism of two-dimensional germanium selenide. *J. Am. Chem. Soc.* **2017**, *139*, 14976−14982.
(19) Zhou, Z.; Long, M.; Pan, L.; Wang, X.; Zhong, M.; Blei, M.; Wang, J.; Fang, J.; Tongay, S.; Hu, W.; Li, J.; Wei, Z. Perpendicular optical reversal of the linear dichroism and polarized photodetection in 2D GeAs. *ACS Nano* **2018**, *12*, 12416−12423.
(20) Song, Q.; Pan, X.; Wang, H.; et al. The in-plane anisotropy of $WTe_2$ investigated by angle-dependent and polarized Raman spectroscopy. *Sci. Rep.* **2016**, *6*, No. 29254.
(21) Beams, R.; Cançado, L. G.; Krylyuk, S.; et al. Characterization of Few-Layer 1T′ $MoTe_2$ by Polarization-Resolved Second Harmonic Generation and Raman Scattering. *ACS Nano* **2016**, *10*, 9626−9636.
(22) Chenet, D. A.; Aslan, O. B.; Huang, P. Y.; et al. In-plane anisotropy in mono- and few-layer $ReS_2$ probed by Raman spectroscopy and scanning transmission electron microscopy. *Nano Lett.* **2015**, *15*, 5667−5672.
(23) Wolverson, D.; Crampin, S.; Kazemi, A. S.; Ilie, A.; Bending, S. J. Raman spectra of monolayer, few-layer, and bulk $ReSe_2$: an anisotropic layered semiconductor. *ACS Nano* **2014**, *8*, 11154−11164.
(24) Gao, W.; Zheng, Z.; Wen, P. T.; Huo, N. J.; Li, J. B. Novel two-dimensional monoelemental and ternary materials: growth, physics and application. *Nanophotonics* **2020**, *9*, 2147−2168.
(25) Wu, J.; Yuan, H.; Meng, M.; Chen, C.; Sun, Y.; Chen, Z.; Dang, W.; Tan, C.; Liu, Y.; Yin, J.; Zhou, Y.; Huang, S.; Xu, H. Q.; Cui, Y.; Hwang, H. Y.; Liu, Z.; Chen, Y.; Yan, B.; Peng, H. High electron mobility and quantum oscillations in non-encapsulated ultrathin semiconducting $Bi_2O_2Se$. *Nat. Nanotechnol.* **2017**, *12*, 530−534.
(26) Li, T.; Tu, T.; Sun, Y.; Fu, H.; Yu, J.; Xing, L.; Wang, Z.; Wang, H.; Jia, R.; Wu, J.; Tan, C.; Liang, Y.; Zhang, Y.; Zhang, C.; Dai, Y.; Qiu, C.; Li, M.; Huang, R.; Jiao, L.; Lai, K.; Yan, B.; Gao, P.; Peng, H. A native oxide high-k gate dielectric for two-dimensional electronics. *Nat. Electron.* **2020**, *3*, 473−478.
(27) Yin, J.; Tan, Z.; Hong, H.; Wu, J.; Yuan, H.; Liu, Y.; Chen, C.; Tan, C.; Yao, F.; Li, T.; Chen, Y.; Liu, Z.; Liu, K.; Peng, H. Ultrafast, highly-sensitive infrared photodetectors based on two-dimensional oxyselenide crystals. *Nat. Commun.* **2018**, *9*, No. 3311.
(28) Yang, T.; Li, X.; Wang, L.; Liu, Y.; Chen, K.; Yang, X.; Liao, L.; Dong, L.; Shan, C. Broadband photodetection of 2D $Bi_2O_2Se$−$MoSe_2$ heterostructure. *J. Mater. Sci.* **2019**, *54*, 14742−14751.
(29) Khan, U.; Luo, Y.; Tang, L.; Teng, C.; Liu, J.; Liu, B.; Cheng, H. Controlled vapor-solid deposition of millimeter-size single crystal 2D $Bi_2O_2Se$ for high-performance phototransistors. *Adv. Funct. Mater.* **2019**, *29*, No. 1807979.
(30) Sun, Y.; Zhang, J.; Ye, S.; Song, J.; Qu, J. Progress Report on Property, Preparation, and Application of $Bi_2O_2Se$. *Adv. Funct. Mater.* **2020**, *30*, No. 2004480.
(31) Eremeev, S. V.; Koroteev, Y. M.; Chulkov, E. V. Surface electronic structure of bismuth oxychalcogenides. *Phys. Rev. B* **2019**, *100*, No. 115417.
(32) Cheng, C.; Wang, M.; Wu, J.; Fu, H.; Chen, Y. Electronic structures and unusually robust bandgap in an ultrahigh-mobility layered oxide semiconductor, $Bi_2O_2Se$. *Sci. Adv.* **2018**, *4*, No. eaat8355.
(33) Xiao, J.; Wang, Y.; Feng, X.; Legut, D.; Wang, T.; Fan, Y. Anisotropic $Bi_2O_2Se$(Te) Monolayer: Realizing Ultra-High Carrier Mobility and Giant Electric Polarization in Two-Dimension. 2019, arXiv:1911.11327. arXiv.org e-Print archive. https://arxiv.org/abs/1911.11327.
(34) Fu, Q.; Zhu, C.; Zhao, X.; Wang, X.; Chaturvedi, A.; Zhu, C.; Wang, X.; Zeng, Q.; Zhou, J.; Liu, F.; Tay, B.; Zhang, H.; Pennycook, S.; Liu, Z. Ultrasensitive 2D $Bi_2O_2Se$ phototransistors on silicon substrates. *Adv. Mater.* **2018**, *1*, No. 1804945.
(35) Huo, N.; Tongay, S.; Guo, W.; Li, R.; Fan, C.; Lu, F.; Yang, J.; Li, B.; Li, Y.; Wei, Z. Novel optical and electrical transport properties in atomically thin $WSe_2/MoS_2$ p−n heterostructures. *Adv. Electron. Mater.* **2015**, *1*, No. 1400066.
(36) Kim, J.; Mastro, A.; Tadjer, J.; Kim, J. Heterostructure $WSe_2$-$Ga_2O_3$ junction field-effect transistor for low-dimensional high-power electronics. *ACS Appl. Mater. Interfaces* **2018**, *10*, 29724−29729.
(37) Huo, N.; Konstantatos, G. Ultrasensitive all-2D $MoS_2$ phototransistors enabled by an out-of-plane $MoS_2$ PN homojunction. *Nat. Commun.* **2017**, *8*, No. 572.
(38) Huo, N.; Gupta, S.; Konstantatos, G. $MoS_2$−HgTe Quantum Dot Hybrid Photodetectors beyond 2 μm. *Adv. Mater.* **2017**, *29*, No. 1606576.
(39) Wang, X.; Li, Y.; Huang, L.; Jiang, X.; Jiang, L.; Dong, H.; Wei, Z.; Li, J.; Hu, W. Short-wave near-infrared linear dichroism of two-dimensional germanium selenide. *J. Am. Chem. Soc.* **2017**, *139*, 14976−14982.
(40) Xin, Y.; Wang, X.; Chen, Z.; Weller, D.; Wang, Y.; Shi, L.; Ma, X.; Ding, C.; Li, W.; Guo, S.; Liu, R. Polarization-Sensitive Self-Powered Type-II GeSe/$MoS_2$ van der Waals Heterojunction Photodetector. *ACS Appl. Mater. Interfaces* **2020**, *12*, 15406−15413.
(41) Xiong, J.; Sun, Y.; Wu, L.; Wang, W.; Gao, W.; Huo, N.; Li, J. High Performance Self-Driven Polarization-Sensitive Photodetectors Based on GeAs/InSe Heterojunction. *Adv. Opt. Mater.* **2021**, *9*, No. 2101017.


https://doi.org/10.1021/acsomega.1c05246
*ACS Omega* 2021, 6, 34763−34770